Journal of Materials Chemistry

PAPER

Branched double-shelled TiO₂ nanotube networks on transparent conducting oxide substrates for dye sensitized solar cells†

Jijun Qiu,[ab] Xiaomin Li,*[b] Xiangdong Gao,[b] Xiaoyan Gan,[b] Binbin Weng,[a] Lin Li,[a] Zijian Yuan,[a] Zhisheng Shi*[a] and Yoon-Hwae Hwang[c]

A novel three-dimensional branched double-shelled TiO₂ nanotube network (3DNTNs) structure was constructed on transparent conducting oxide substrates (TCO) by using a ZnO-nanorod array template-assisted method. Various morphological features, such as branch length and population density, could be easily tailored by simply modifying the growth time. The performances of dye-sensitized solar cells (DSCs) fabricated with TiO₂ 3DNTNs are higher than those assembled with 1-dimensional nanotube arrays. The hollow branches filling in the spaces between the double-shelled stem nanotubes increase the amount of dye-loading, resulting in an enhanced light-harvesting ability.

1. Introduction

The discovery of one-dimensional (1D) carbon nanotubes (CNTs) triggered the design and fabrication of nanostructures of functional materials.[1] Nowadays, the precise synthesis of complex inorganic nanostructures with controllable sizes and dimensions is an essential step toward the realization of multi-functionality of nanosystems.[2–6] To date, various nanostructures, including zero dimensional (0D)[7–9] multi-shelled spheres, one-dimensional 1D[2–6,10–15] multi-shelled tubes, two-dimensional (2D)[16–20] heterogeneous nanofilms, and three-dimensional (3D)[21–34] ordered mesoporous materials and hierarchical networks have been reported, and are so attractive, not only because of their fantastic interior architectures, but also importantly due to their variation in the physicochemical properties caused by interfacial effects, which can lead to many potential applications. In particular, 3D hierarchical networks are attractive for many nanoscale devices, especially those for which a large surface area and surface energy are desirable. Furthermore, the network structures also can improve the nanoscale devices' mechanical stability, due to their structural interconnectivities,[3] which avoids the possibility of aggregation to maintain a large surface area with a small thickness.

In recent years, 3D branched nanowire network structures of functional materials like Pt,[21] ZnO,[22–28] TiO₂,[29–31] WO₃,[32] V₂O₅,[33] SnO₂,[34] Fe₂O₃,[35] MnO₂,[36] PbSe,[37] and FeSi[38] were successfully synthesized using the sequential seeding of catalysts and the self-assembled growth of nanowires, and exhibited dramatic potential in improving performance for applications in solar cells, energy storage, sensors, field emitters, *etc*. For example, it has been demonstrated that hierarchical ZnO[22–28] and TiO₂[29–31] nanowire networks can significantly increase the conversion efficiency of dye-sensitized solar cells (DSCs) due to an increased light harvesting ability, which originates from a large dye-loading capability and the multiple light scattering of the branched structures. In order to further improve the performance of devices and meet the needs of their applications, the development of 3D branched nanowire networks will focus on optimizing and designing new 3D branched structures.

Herein, a 3D branched nanotube network (3DNTNs) structure was proposed as a derived structure of a 3D branched network. Compared with nanowire networks, 3DNTNs have the obvious advantages of larger specific surface area and multi-level interior structures, due to the hollow channels of the nanotubes. However, these hollow channels are also the major factor that makes the synthesis of branched NTNs a great technical challenge. To the best of our knowledge, there is no report on inorganic branched 3DNTNs for nanoscale devices.

Based on previous works on the fabrication of simple single and multiple shelled TiO₂ nanotube arrays,[39,40] we report a facile synthetic route to fabricate branched double-shelled TiO₂ 3DNTNs on transparent conductive substrates by using a ZnO nanorod (NR) template-directed method. This synthetic strategy shows distinct advantages, such as large-scale production, being environmentally friendly, low cost, and having precise structural

ᵃSchool of Electrical and Computer Engineering, University of Oklahoma, Norman, Oklahoma, 73019, USA. E-mail: shi@ou.edu; Fax: +1-405-325-7066; Tel: +1-405-325-4292

ᵇState Key Laboratory of High Performance Ceramics and Superfine Microstructures, Shanghai Institute of Ceramics, Chinese Academy of Sciences, Shanghai 200050, China. E-mail: lixm@mail.sic.ac.cn; Fax: +86-21-5241-3122; Tel: +86-21-5241-2554

ᶜDepartment of Nanomaterials Engineering & BK 21 Nano Fusion Technology Division, Pusan National University, Miryang 627-706, Korea

† Electronic supplementary information (ESI) available: Fig. S1 shows the growth direction of ZnO branches; Fig. S2 shows a narrow diameter distribution of ZnO branches; Fig. S3 shows a scattering effect at the top surfaces of 1D nanotube arrays and 3D networks. Fig. S4 shows the connection between TiO₂ nanotubular stems and the FTO substrate before LbL-AR deposition. See DOI: 10.1039/c2jm34574a
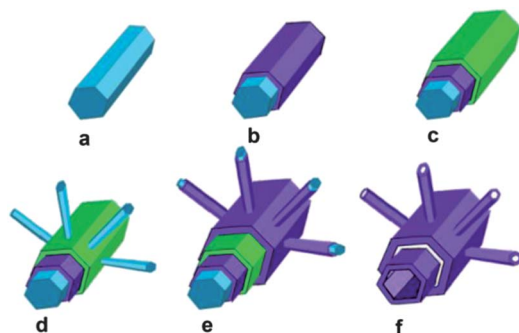
This journal is © The Royal Society of Chemistry 2012

J. Mater. Chem., 2012, **22**, 23411–23417 | 23411

control and good reproducibility. The branched TiO_2 3DNTNs-based DSCs exhibited a higher conversion efficiency than that of the 1D TiO_2 nanotube-based DSCs, resulting from the enhanced surface area and dye loading due to the small size of the TiO_2 branches.

2. Experimental

2.1. Fabrication of the branched double-shelled TiO_2 3DNTNs

The overall synthetic strategy is illustrated in Scheme 1. The first step is to fabricate well-aligned ZnO nanorod (NR) stems perpendicular to the transparent conducting F:SnO$_2$ (FTO) substrates using a hydrothermal technique. Then, every pristine ZnO NR stem is covered by a TiO_2 nanoparticle film via a layer-by-layer absorption and reaction (LbL-AR) backfill approach to form TiO_2–ZnO shell–core structures, as shown in Scheme 1b. Next, ZnO nanoparticle films are deposited over the first TiO_2 shells using a sol–gel method, as shown in Scheme 1c. The ZnO thin films act as both sacrificial spacers between the double TiO_2 shells, and as seed layers to induce the growth of the ZnO nanowire (NW) branches along the radial direction of the ZnO NR stems, as shown in Scheme 1d. Subsequently, the LbL-AR backfill approach is employed again to assemble the second TiO_2 stem shells and the radial TiO_2 branch shells, as shown in Scheme 1e. Finally, the branched double-shelled TiO_2 3DNTNs, as shown in Scheme 1f, are obtained after removing the ZnO NR templates and ZnO sacrificial spacers using selective wet-chemical etching.

2.1.1. First hydrothermal growth of the ZnO NR stem templates.
0.075 mol Zn(CH$_3$COO)$_2$·2H$_2$O and 0.075 mol mon-oethanolamine were dissolved in 100 ml 2-methoxyethanol solution to yield a clear and homogeneous ZnO sol. Then cleaned FTO/glass substrates (TCE 15) were slowly immersed into the ZnO sol followed by removal at a withdrawal rate of 3.0 cm min^{-1} to form ZnO gel layers on the FTO surfaces. Subsequently the

ZnO gel film coated FTO substrates were heated to 550 °C for 1 h to obtain the oriented ZnO seed layers.

The ZnO seeded FTO/glass substrates were transferred into a 95 °C growth solution prepared from dissolving zinc nitrate hexahydrate, hexamethylenetetramine and polyethylenimine in distilled (DI) water, with a concentration ratio of 0.02 : 0.02 : 0.0005, and kept at 95 °C without any stirring. The hot solution was refreshed every 12 h for a sufficient growth rate of 0.4–0.5 μm h^{-1}, until the desired lengths were achieved.

2.1.2. First LbL-AR deposition of the first TiO_2 shell.
A layer-by-layer absorption and reaction technique was employed to deposit a TiO_2 shell on the ZnO NR templates, reported in ref. 39 and 40. In brief, the ZnO NR stem templates on the FTO substrates were successively immersed in 0.5 M TiO_2 sol, ethanol, water, and ethanol to form the TiO_2 nanoparticle shells around the ZnO NR stems. Then the above procedure was repeated several times (typically 25 times) to obtain the desired shell thickness. The obtained TiO_2–ZnO shell–core stem templates were calcined at 300 °C for 1 h to remove the organic residue.

2.1.3. Sol–gel formation of the ZnO spacers/seed layers.
The TiO_2 coated ZnO NR stem templates were immersed again into a ZnO sol for 10 s at room temperature, and withdrawn at a speed of 2.0 cm min^{-1} to form a ZnO gel film over the NR stems, follow by heating at 300 °C for 10 min. Subsequently, the sol–gel deposition and baking procedures were repeated several times (typically 8 times) to obtain the desired thickness. Finally, the samples were calcined at 500 °C for 1 h.

2.1.4. Second hydrothermal growth of the radial ZnO branches.
This step was the same as the first hydrothermal growth step, see section 2.1.1 above.

2.1.5. Second LbL-AR deposition of the second TiO_2 shell and the TiO_2 nanotubular branches.
This step was a repeat of the procedure in section 2.1.2, followed by a heat treatment at 450 °C for 1 h.

2.1.6. Wet-chemical etching method to form the TiO_2 nanotube networks.
The branched ZnO NR templates and ZnO spacers were removed by immersing them in 0.015 M TiCl$_4$ aqueous solution for 1.5 h at room temperature. Then the hollow nanotubular networks were repeatedly rinsed with DI water to remove residual absorbed zinc ions.

2.2. Assembly of branched double-shelled TiO_2 NTNs based DSCs

2.2.1. Enhancement of adhesion by LbL-AR deposition.
Before being assembled into DSCs, the branched TiO_2 3DNTNs samples were coated with a TiO_2 sol by using LbL-AR deposition again to further enhance the adhesion between the networks and the FTO substrates, followed by annealing at 500 °C for 1 h.

2.2.2. TiCl$_4$ treatment of double shelled TiO_2 3DNTNs.
The prepared TiO_2 3DNTNs were shaped into a fixed circular shape of area 0.42 cm^2, and transferred into a 70 °C TiCl$_4$ solution (0.04 M) for 1 h, followed by a heat treatment at 500 °C for 1 h.

Scheme 1 Schematic illustration of the synthetic process for branched double-shelled TiO_2 3D nanotubular networks (3DNTNs). (a) Synthesis of ZnO nanorod (NR) stems by a hydrothermal method; (b) deposition of the first TiO_2 stem shells by a layer-by-layer absorption and reaction (LbL-AR) technique; (c) coating with ZnO sacrificial spacers by a sol–gel method; (d) growth of radial ZnO nanowire (NW) branches by a second hydrothermal growth; (e) deposition of the second TiO_2 stem shells and radial branch shells by using a second LbL-AR step and (f) removal of the ZnO NR template and spacers by selective chemical etching.

2.2.3. Assembly of the DSCs. The annealed TiO_2 3DNTNs were sensitized with a 0.5 mM N719–ethanol solution for 12 h at room temperature. 50 nm platinum covered FTO substrates were used as the counter-electrodes and sealed with the TiO_2 3DNTNs photoanodes into sandwich cells by hot melt plastic spacers with 100 μm thickness. The electrolyte, made up of BMII (0.6 M), I_2 (0.03 M), TBP (0.5 M), and GuSCN (0.1 M) in a mixture of acetonitrile and valeronitrile, was introduced into the internal space by a syringe and the capillary effect.

2.3. Characterizations of the branched double-shelled TiO_2 3DNTNs based DSCs

2.3.1. Structural characterization of the TiO_2 3DNTNs. XRD analysis for phase identification was performed using a Bruker AXS D8 Advance diffractometer with CuKα radiation. The structural characteristics of the branched nanotube networks were observed by field-emission scanning electron microscopy (FESEM, Hitachi S-4700) and transmission electron microscopy (TEM, JEOL JEM-2100F). BET surface areas and pore size distributions were characterized by using a Micrometerics ASP2000 surface area analyzer. The amount of adsorbed dye was measured by immersing the films in 0.1 M NaOH solution and measuring the optical absorbance with a spectrophotometer (Shimadzu UV-3101PC).

2.3.2. Photovoltaic characterization of the DSCs. The TiO_2 nanotube network based DSCs were tested on an electrochemical workstation (CHI-660B), using simulated AM 1.5 illumination (100 mW cm^{-2}) provided by an Oriel simulator (300W, 91160B). J–V curves were measured by sweeping the bias voltage in the range 0 to 0.85 V. A mask of 0.42 cm^2 as the photoanode area was employed during the characterization for calibration of the cell area.

3. Results and discussion

The whole fabrication process was firstly characterized using normalized XRD spectrum analysis, as shown in Fig. 1. In a typical XRD pattern of the ZnO NR stem templates obtained by
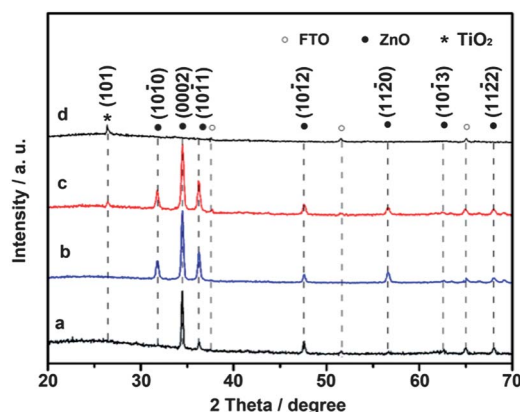

Fig. 1 Normalized XRD spectra recorded at different fabrication stages. XRD patterns of (a) ZnO NR stem templates obtained from the first hydrothermal growth; (b) branched ZnO NR templates after the second hydrothermal growth; (c) TiO_2 shell coated branched ZnO NR templates after LbL-AR TiO_2 deposition and (d) branched double-shelled TiO_2 3DNTNs after removing the branched ZnO templates by wet-etching.

the hydrothermal method, as shown in Fig. 1a, the 6 diffraction peaks are respectively indexed to the (0002), (10$\bar{1}$1), (10$\bar{1}$2), (11$\bar{2}$0), (10$\bar{1}$3) and (11$\bar{2}$2) planes of wurtzite phase ZnO. The dominant (0002) peak and the large intensity ratio of (0002) : (10$\bar{1}$1) suggest that the ZnO NR stems grew along the c-axis orientation normal to the FTO surface. After the growth of the radial ZnO NW branches, a new peak is observed at 31.76° in Fig. 1b, indexed to ZnO (10$\bar{1}$0) plane. At the same time, the intensity of the (10$\bar{1}$1) plane shows an obvious increase compared with the intensity of the ZnO NR stem templates. The appearance of the ZnO (10$\bar{1}$0) plane and the decreased intensity ratio of (0002) : (10$\bar{1}$1) strongly indicates the formation of branched ZnO NR structures. After LbL-AR deposition, TiO_2 shells were successfully coated onto the branched ZnO NR templates, as suggested by a peak at 25.5° indexed to the anatase-TiO_2 (101) plane, shown in Fig. 1c. After selective chemical etching, except for the TiO_2 (101) peak, all of peaks related to the branched ZnO NR templates vanished, indicating a thorough removal of the ZnO templates. The presence of the TiO_2 (101) peak suggests that the TiO_2 shells can survive the diluted $TiCl_4$ etching solution, ensuring the formation of branched TiO_2 3DNTNs on the FTO substrates.

The corresponding FESEM images recorded at different formation stages give clearer evidence for the XRD patterns, as shown in Fig. 2 and 3. Fig. 2a shows the side-view FESEM images of a typical ZnO NR stem template after the first hydrothermal growth. It shows that the ZnO NR stems are perpendicular to the FTO substrate, with a diameter in the range of 400–600 nm and a length of 30 μm. The magnified FESEM image of an individual ZnO NR in the inset of Fig. 2a shows a hexagonal cross section with smooth surfaces. After LbL-AR deposition, the ZnO NR stems were coated by smooth TiO_2 shells, as shown in Fig. 2b (the detailed structural features are characterized in Fig. 2i). After the deposition of ZnO spacers using the sol–gel method, the high magnification FESEM image of the ZnO spacer coated stems, as shown in Fig. 2c, reveals that TiO_2–ZnO shell–core NR stems are completely covered by a continuous and compact ZnO coating, which is composed of ZnO nanoparticle aggregates with a mean diameter of about 15 nm. It should be noted that the first TiO_2 shell is of great benefit to the formation of continuous compact ZnO sacrificial spacers on the ZnO NR stems by electrostatic interaction with the ZnO sol–gel, which is of crucial importance for the synthesis of branched double-shelled TiO_2 nanotubular structures. Without forming a continuous ZnO sacrificial spacer, in our case, longer ZnO NR stems are obtained after the second hydrothermal growth, rather than a hierarchical branched ZnO NR configuration. After the second hydrothermal growth, a branched ZnO NR structure is obtained, as shown in Fig. 2d–g. The low-magnification side- and top-view FESEM images in Fig. 2d and e show that the radial branches are grown from each ZnO spacer coated TiO_2–ZnO shell–core NR stem over the entire substrate with a density of 10^7 cm^{-2}, indicating a high uniformity and yield. The high magnification side-view FESEM image in Fig. 2g and the TEM image in Fig. 2h show that the ZnO branches grow vertically from the NR template and have a uniform diameter of 50 nm. More structural characterizations of the branched ZnO template are shown in Fig. S1 in the ESI.† Notably, the length of the radial ZnO NW branches decreases
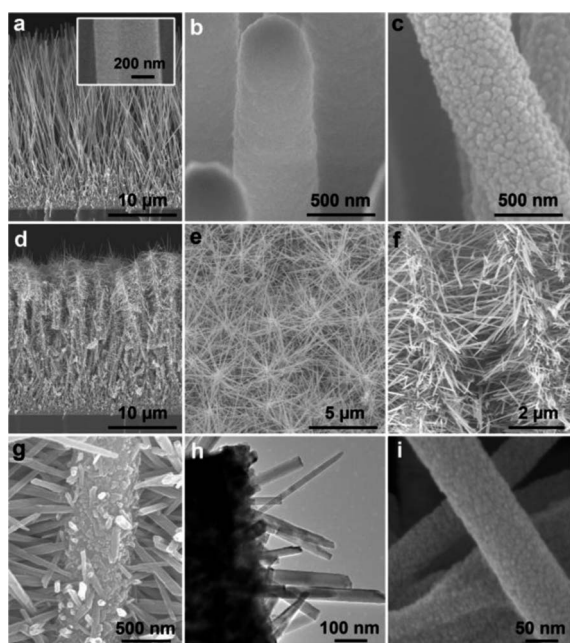
Fig. 2 Typical FESEM and TEM images of the ZnO NR templates observed at different fabrication stages. (a) Low and high (inset) magnification side-view images of the vertical ZnO NR stem template obtained from the first hydrothermal growth; (b) high magnification side-view FESEM of TiO$_2$–ZnO shell–core structures after LbL-AR deposition; (c) high magnification FESEM image of ZnO spacers coated TiO$_2$–ZnO shell–core NR stem templates after ZnO sol–gel deposition; (d) low magnification side-view and (e) top-view, and (f) middle and (g) high magnification side-view FESEM images and (h) middle magnification TEM image of branched ZnO NR templates after the second hydrothermal growth, and (i) high magnification FESEM image of the TiO$_2$ shell coated ZnO branches after the second TiO$_2$ LbL-AR deposition.
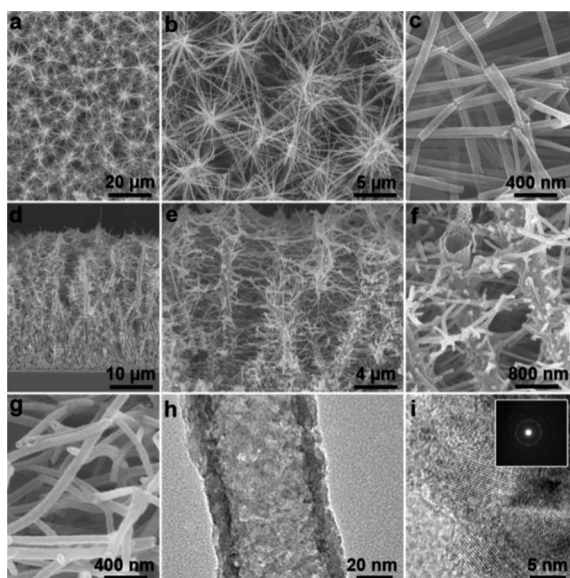

Fig. 3 Typical FESEM and TEM images of TiO$_2$ 3DNTNs. (a–c) top- and (d–f) side-view FESEM images with low (a and d), middle (b and e) and high magnification (c and f); magnified FESEM image of TiO$_2$ branches pictured at the bottom of the stems; (h) TEM, (i) HRTEM image and SAED (inset) of a TiO$_2$ nanotubular branch.

from 2 to 1 μm along the axial direction of the ZnO NR stems from top to the bottom. The decreased length is attributed to the insufficient supply resulting from the decreased ion exchange route, where the fresh growth solution hardly infiltrates into the deep side-wall of the ZnO stems due to the space blocking effect. Finally, the radial ZnO NW branches are completely covered by compact TiO$_2$ nanoparticles with a diameter of 5–8 nm after the second LbL-AR TiO$_2$ deposition, as shown in Fig. 2i, indicating the good copy-shaping ability and processability of curved surfaces of the LbL-AR method.

Fig. 3 shows the typical FESEM images of the TiO$_2$ 3DNTNs. The low-magnification top-view FESEM image of the TiO$_2$ 3DBNTNs, as shown in Fig. 3a, reveals an intact network architecture even after the removal of the branched ZnO NR templates. The middle magnification top-view FESEM image in Fig. 3b further confirms that the network architecture is constructed by lateral interpenetration of the TiO$_2$ nanotubular branches radiating from the corresponding TiO$_2$ tube stems perpendicular to the FTO substrate. Every individual TiO$_2$ branch has a hollow structure with an outer diameter of 60 nm, as shown in Fig. 3c. The side-view FESEM images in Fig. 3d and e show that the TiO$_2$ nanotubular stems still stand vertically on the FTO substrate, showing the structural stability of the TiO$_2$ 3DNTNs. The middle side-view FESEM image of a broken TiO$_2$ nanotubular stem, shown in Fig. 3f, clearly reveals a double-shelled (tube-in-tube) nanostructure with a shell thickness of about 15 nm. The high magnification FESEM image (Fig. 3g) of the TiO$_2$ branches pictured from the bottom of the TiO$_2$ nanotube stems shows a hollow tubular nanostructure with smooth surfaces, indicating that the ZnO branches have been completely removed. The tubular structure of the TiO$_2$ branches was further confirmed by TEM and HRTEM images, as shown in Fig. 3h and i. The TEM image in Fig. 3h apparently shows a completely hollow channel and a uniform wall thickness of 10 nm, indicating the excellent structural control of the LbL-AR route. At the same time, the disordered porous nature of the TiO$_2$ shell is observed in Fig. 3h. The HRTEM image shown in Fig. 3i reveals that the porous structure is attributed to the loose stacking of polycrystalline anatase TiO$_2$ nanoparticles with a diameter of 4–6 nm.

The porous structure was also confirmed by the N$_2$ adsorption–desorption isotherms of TiO$_2$ 3DNTNs peeled-off from the FTO substrates, as shown in Fig. 4. It shows typical IV curves with H1 hysteresis loops, indicating the presence of both mesopores and macropores. Based on the FESEM and TEM images, the mesoporous structure, which was characterized at relative pressures of 0.45–0.8, derives from the non-close-packed structure of TiO$_2$ nanocrystallites, and the macroporous structure at high relative pressure of 0.9–1.0 is ascribed to the large inner channels of the TiO$_2$ stems and branches. The Barrett–Joyner–Halenda (BJH) pore diameter distribution plot shows a narrow size distribution centered at 2.9 nm, and the Brunauer–Emmett–Teller (BET) specific surface area is ~120 m^2 g^{-1}. These results are in agreement with those of double-shelled TiO$_2$ nanotube arrays obtained by a ZnO template-assisted LbL-AR method.[40] The larger specific surface area of 3DNTNs (50 m^2 g^{-1} for the TiO$_2$ nanorod arrays[41]) is caused by its hollow structure.

Although both the XRD and FESEM results show that the branched ZnO NR templates were completely removed by the etching solution, the energy dispersive spectrum (EDS) in Fig. 5
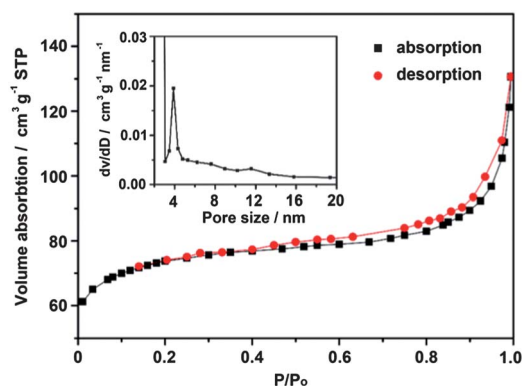

Fig. 4 N_2 adsorption–desorption isotherm plots and pore size distribution curve (inset) of the TiO$_2$ 3DNTNs.

Fig. 6 FESEM images of TiO$_2$ 3DNTNs with various population densities and lengths of the TiO$_2$ branches. (a–c) Top-view and (d–f) side-view FESEM images of TiO$_2$ 3DNTNs fabricated with a second hydrothermal growth of 24 h (a and d), 48 h (b and e) and 96 h (c and f).

shows there was about 2.53% zinc element remaining in the TiO$_2$ 3DNTNs, which is attributed to the absorption of Zn^{2+} by the TiO$_2$ 3DNTNs due to their porous structure and large surface area.

For the template-directed strategy, it is critical to obtain templates with desired architectures, controllable sizes and physical dimensions, since the subsequent coating will inherit the geometrical features of the templates. Except for low cost, facile large-scale production and good reproducibility, the hydrothermal method also shows a distinct advantage in precisely modulating the structural features of the branched ZnO NR templates and the resultant TiO$_2$ 3DNTNs, such as length, diameter, population density, *etc.* Fig. 6 shows the typical top- and side-view middle magnification FESEM images of TiO$_2$ 3DNTNs with different population densities and lengths of radial TiO$_2$ branches, which were inherited from the corresponding branched ZnO templates by simply tuning the second hydrothermal growth time from 12 to 48 h. Obviously, the population density and the length of the ZnO branches increase roughly linearly with the second hydrothermal growth time. The growth rate of the ZnO branches is about one third of the growth rate of the ZnO NR stems, at about 0.5 μm h^{-1}, due to the space blocking effect.

The branched TiO$_2$ 3DNTNs with various radial branch lengths were employed as anodes to assemble DSCs. The current density (J)–voltage ($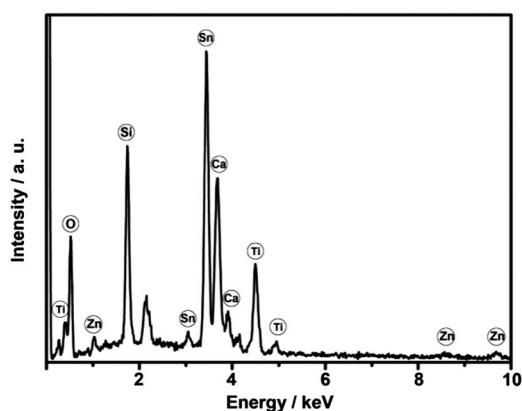V$) characteristics of the three DSCs are shown in Fig. 7, and the photovoltaic parameters are summarized in Table 1. Compared with the double-shelled TiO$_2$ nanotube arrays, the branched double-shelled TiO$_2$ 3DNTNs improve the conversion efficiency of the DSCs from 4.42 to 5.33%, due to the increase of J_{sc} from 8.2 to 11.9 mA cm^{-1}. At the same time, a corresponding increase in J_{sc} from 11.9 to 13.7 and η from 5.33 to 5.74% is observed with an increase of the radial branch length from 2 to 5 μm. As the scattering effect was observed in both 1D TiO$_2$ nanotube arrays and the TiO$_2$ 3DNTNs, as shown in Fig. S3 in the ESI,† in our opinion the improved performance of the 3DNTNs DSCs is attributed to the increased surface area resulting from the TiO$_2$ nanotubular branches with small size. This is confirmed by the increased dye loading from 3.86 to 7.27×10^{-8} mol cm^{-2}, as shown in Table 1. The V_{oc} decreases from 0.84 to 0.75 V with an increase in the length of the TiO$_2$ nanotubular branches. The drop in V_{oc} with increasing length of TiO$_2$ branches is similar to previous reports that the V_{oc} tends to decrease with increasing the thicknesses of TiO$_2$ nanotubular and nanoparticle photoanodes.[42,43] Based on our previous research, the deteriorated V_{oc} is a result of the increase in charge-recombination sites provided by increase of the branch length, resulting in an increased transport resistance.[39] It is important to note that the DSCs' performances also depend on the residual

Fig. 5 A typical energy dispersive spectrum (EDS) of the TiO$_2$ 3DNTNs after immersing in 0.015 M TiCl$_4$ etching solution and DI water for 1.5 h.
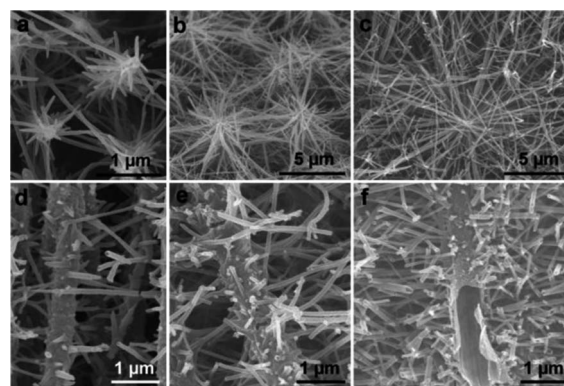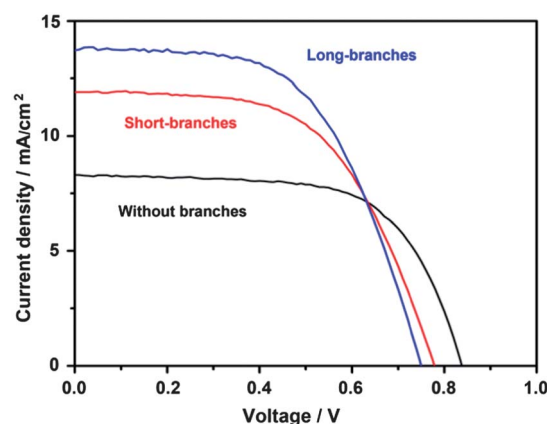

Fig. 7 J–V characteristics of DSCs made of branched double-shelled TiO$_2$ 3DNTNs with various branch lengths. The $[Zn^{2+}]$ in the TiO$_2$ 3DNTNs is lower than 2%.

Table 1 Photovoltaic parameters of DSCs made of branched double-shelled TiO$_2$ 3DNTNs with various lengths

Branch length (μm)	V_{OC} (V)	J_{sc} (mA cm^{-2})	FF (%)	η (%)	D (mol cm$^{-2} \times 10^{-8}$)
0	0.84	8.2	63	4.42	3.86
2	0.78	11.9	57	5.33	5.14
5	0.75	13.7	55	5.74	7.27

[Zn^{2+}] in the TiO$_2$ 3DNTNs. This behavior is attributed to the formation of Zn^{2+}-dye complexes due to long immersion times in ruthenium-based dye solution.[44,45] This undesired chemical reaction deteriorates the TiO$_2$ surface, resulting in aggregation of dye molecules at the TiO$_2$ surface, which hinders charge separation and prevents efficient injection of electrons.[46–48] Therefore, it is necessary to decrease the residual zinc ion concentration to a minimum for a high DSCs performance. However, the most effective procedures to decrease [Zn^{2+}], involving extended etching and rinsing times in diluted TiCl$_4$ aqueous solution and DI water respectively, may lead to a poor adhesion between TiO$_2$ 3DNTNs and the FTO substrate, even peeling off the TiO$_2$ networks from the substrates. To reinforce adhesion for high DSCs conversion efficiency, 5-cycle LbL-AR TiO$_2$ deposition can be employed once again after removing the branched ZnO template, which has a negligible effect on the morphology of the TiO$_2$ 3DNTNs. The reason is shown in the ESI in Fig. S4.† Additionally, the performance of the TiO$_2$ 3DNTNs DSCs currently is lower than that of traditional TiO$_2$ nanoparticle DSCs, resulting from a low space-utilization-efficiency due to the fact that the inner channels of the TiO$_2$ stems with large diameter are not fully utilized yet in this case. Therefore, how to decrease the diameter of the ZnO NR stems and how to fully utilize the empty channels will be a challenge for the ZnO NR template assisted LbL-AR method of TiO$_2$ 3DNTNs.

4. Conclusions

In summary, this work presents the fabrication of branched double-shelled TiO$_2$ 3DNTNs on a TCO substrate by a ZnO NR template assisted LbL-AR method, and investigates the technological parameters of the performances of TiO$_2$ 3DNTNs based DSCs. The experimental results show that the branched TiO$_2$ 3DNTNs can noticeably improve the DSCs' performance, resulting from the enhanced surface area and the higher dye loading due to the radial TiO$_2$ branches with small diameter. Additionally, in ensuring good adhesion, a decrease in the residual [Zn^{2+}] is beneficial for the improvement of the performance of the DSCs. The potential of such an approach for synthesizing complex 3D nanotubular networks has not been fully explored, and it is believed that optimizing the processing parameters and making full use of the inner channels of the nanotubular stems will further increase the internal surface area, allowing DSCs with better performance to be fabricated.

Acknowledgements

References

1 S. Iijima, *Nature*, 1991, **354**, 56.
2 M. J. Bierman and S. Jin, *Energy Environ. Sci.*, 2009, **2**, 1050.
3 R. Liu, J. Duaya and S. B. Lee, *Chem. Commun.*, 2011, **47**, 1384.
4 C. Cheng, B. Liu, H. Yang, W. Zhou, L. Sun, R. Chen, S. F. Yu, J. Zhang, H. Gong, H. Sun and H. J. Fan, *ACS Nano*, 2009, **3**, 3069.
5 C. Cheng, Y. Y. Tay, H. H. Hng and H. J. Fan, *J. Mater. Res.*, 2011, **26**, 2254.
6 J. Liu, C. I. Cheng, W. Zhou, H. Lia and H. J. Fan, *Chem. Commun.*, 2011, **47**, 3436.
7 X. W. Lou, L. A. Archer and Z. Yang, *Adv. Mater.*, 2008, **20**, 3987.
8 X. W. Lou, C. Yuan and L. A. Archer, *Small*, 2007, **3**, 261.
9 J. S. Chen, D. Luan, C. M. Li, F. Yin, C. Boey, S. Qiao and X. W. Lou, *Chem. Commun.*, 2010, **46**, 8252.
10 H. M. Cheng, W. H. Chiu, C. H. Lee, S. Y. Tsai and W. F. Hsieh, *J. Phys. Chem. C*, 2008, **112**, 16359.
11 S. H. Ko, D. Lee, H. W. Kang, K. H. Nam, J. Y. Yeo, S. J. Hong, C. P. Grigoropoulos and H. J. Sung, *Nano Lett.*, 2011, **11**, 666.
12 J. H. Jung, T. Shimizu and S. Shinkai, *J. Mater. Chem.*, 2005, **15**, 3979.
13 W. Zhang, Z. Xi, G. Li, Q. Wang, H. Tang, Y. Liu, Y. Zhao and L. Jiang, *Small*, 2009, **5**, 1742.
14 S. P. Albu, A. Ghicov, S. Adabelrgenova, P. Drechsel, D. LeClere, G. E. Thompson, J. M. Macak and P. Schmuki, *Adv. Mater.*, 2008, **20**, 4135.
15 C. Bae, Y. Yoon, H. Yoo, D. Han, J. Cho, B. H. Lee, M. M. Sung, M. G. Lee, J. Kim and H. Shin, *Chem. Mater.*, 2009, **21**, 2574.
16 D. H. Wang, D. W. Choi, J. Li, Z. G. Yang, Z. M. Nie, R. Kou, D. H. Hu, C. M. Wang, L. V. Saraf, J. G. Zhang, I. A. Aksay and J. Liu, *ACS Nano*, 2009, **3**, 907.
17 D. W. Wang, F. Li, J. P. Zhao, W. C. Ren, Z. G. Chen, J. Tan, Z. S. Wu, I. Gentle, G. Q. Lu and H. M. Cheng, *ACS Nano*, 2009, **3**, 1745.
18 Q. Wu, Y. X. Xu, Z. Y. Yao, A. R. Liu and G. Q. Shi, *ACS Nano*, 2010, **4**, 1963.
19 S. M. Paek, E. Yoo and I. Honma, *Nano Lett.*, 2009, **9**, 72.
20 K. Zhang, L. L. Zhang, X. S. Zhao and J. S. Wu, *Chem. Mater.*, 2010, **22**, 1392.
21 M. Rauber, I. Alber, S. Muller, R. Neumann, O. Picht, C. Roth, A. Schokel, M. E. Toimil-Molares and W. Ensinger, *Nano Lett.*, 2011, **11**, 2304.
22 P. X. Gao, C. S. Lao and Z. L. Wang, *Chem. Phys. Lett.*, 2005, **408**, 174.
23 Q. Zhang and G. Cao, *Nano Today*, 2011, **6**, 91.
24 C. T. Wu and J. J. Wu, *J. Mater. Chem.*, 2011, **21**, 13605.
25 K. Sun, Y. Jing, C. Li, X. Zhang, R. Aguinaldo, A. Kargar, K. Madsen, K. Banu, Y. Zhou, Y. Bando, Z. Liu and D. Wang, *Nanoscale*, 2012, **4**, 1515.
26 I. Herman, J. Yeo, S. Hong, D. Lee, K. H. Nam, J. Choi, W. Hong, D. Lee, C. P. Grigoropoulos and S. H. Ko, *Nanotechnology*, 2012, **23**, 194005.
27 M. McCune, W. Zhang and Y. Deng, *Nano Lett.*, 2012, **12**, 3656.
28 H. Y. Chen, D. B. Kuang and C. Y. Su, *J. Mater. Chem.*, 2012, **22**, 15475.
29 J. Shi, Y. Hara, C. Sun, M. A. Anderson and X. Wang, *Nano Lett.*, 2011, **11**, 3413.
30 F. Shao, J. Sun, L. Gao, S. Yang and J. Luo, *J. Mater. Chem.*, 2012, **22**, 6824.
31 W. P. Liao and J. J. Wu, *J. Mater. Chem.*, 2011, **21**, 9255.
32 A. Ponzoni, E. Comini, G. Sberveglieri, J. Zhou, S. Z. Deng, N. Sheng Xu, Y. Ding and Z. L. Wang, *Appl. Phys. Lett.*, 2006, **88**, 203101.
33 Z. Chen, Y. Qin, D. Weng, Q. Xiao, Y. Peng, X. Wang, H. Li, F. Wei and Y. Lu, *Adv. Funct. Mater.*, 2009, **19**, 3420.

34 J. X. Wang, D. F. Liu, X. Q. Yan, H. J. Yuan, L. J. Ci, Z. P. Zhou, Y. Gao, L. Song, L. F. Liu, W. Y. Zhou, G. Wang and S. S. Xie, *Solid State Commun.*, 2004, **130**, 89.

35 W. Zhou, C. Cheng, J. Liu, Y. Y. Tay, J. Jiang, X. Jia, J. Zhang, H. Gong, H. H. Hng, T. Yu and H. J. Fan, *Adv. Funct. Mater.*, 2011, **21**, 2439.

36 J. Liu, J. Jiang, M. Bosman and H. J. Fan, *J. Mater. Chem.*, 2012, **22**, 2419.

37 M. J. Bierman, Y. K. A. Lau and S. Jin, *Nano Lett.*, 2007, **7**, 2907.

38 R. S. Jeannine and J. Song, *J. Mater. Chem.*, 2010, **20**, 1375.

39 J. Qiu, F. Zhuge, K. Lou, X. Gao, X. Gan, W. Yu and X. Li, *J. Mater. Chem.*, 2011, **21**, 5062.

40 J. Qiu, X. Li, X. Gao, X. Gan, L. Li, B. Weng and Z. Shi, *J. Mater. Chem.*, 2012, **22**, 3549.

41 Y. Liao, W. Que, Q. Jia, Y. He, J. Zhang and P. Zhong, *J. Mater. Chem.*, 2012, **22**, 7937.

42 K. Shankar, G. K. Mor, H. E. Prakasam, S. Yoriya, M. Paulose, O. K. Varghese and C. A. Grimes, *Nanotechnology*, 2007, **18**, 065707.

43 D. Kim, A. Ghicov and P. Schmuki, *Electrochem. Commun.*, 2008, **10**, 1835.

44 K. Keis, J. Lindgren, S. E. Lindquist and A. Hagfeldt, *Langmuir*, 2000, **16**, 4688.

45 T. P. Chou, Q. F. Zhang and G. Z. Cao, *J. Phys. Chem. C*, 2007, **111**, 18804.

46 J. A. Anta, E. Guillen and R. Tena-Zaera, *J. Phys. Chem. C*, 2012, **116**, 11413.

47 R. Katoh, A. Furube, Y. Tamaki, T. M. YoshiharaMurai, K. Hara, S. Murata, H. Arakawa and M. Tachiya, *J. Photochem. Photobiol., A*, 2004, **166**, 69.

48 T. Horiuchi, H. Miura, K. Sumioka and S. Uchida, *J. Am. Chem. Soc.*, 2004, **126**, 12218.

This journal is © The Royal Society of Chemistry 2012

J. Mater. Chem., 2012, **22**, 23411–23417 | 23417